Phys. Status Solidi B **247**, No. 5, 1001–1015 (2010) / **DOI** 10.1002/pssb.200945579

physica status solidi b
www.pss-b.com
basic solid state physics

Feature Article

Ultrathin magnesia films as support for molecules and metal clusters: Tuning reactivity by thickness and composition

Mihai E. Vaida[1], Thorsten M. Bernhardt*[,1], Clemens Barth[2], Friedrich Esch[3], Ueli Heiz[3], and Uzi Landman[4]

[1] Institute of Surface Chemistry and Catalysis, University of Ulm, Albert-Einstein-Allee 47, 89069 Ulm, Germany
[2] CINAM-CNRS, Campus de Luminy, Case 913, 13288 Marseille Cedex 09, France
[3] Department of Chemistry, Technical University of Munich, Lichtenbergstraße 4, 85748 Garching, Germany
[4] School of Physics, Georgia Institute of Technology, Atlanta, Georgia 30332-0430, USA

Received 1 December 2009, accepted 10 February 2010
Published online 24 March 2010

PACS 68.47.Jn, 79.60.–i, 82.53.Eb, 82.53.St

* Corresponding author: e-mail thorsten.bernhardt@uni-ulm.de, Phone: +49 731 50 25455, Fax: +49 731 50 25452

Ultrathin metal oxide films have attracted considerable interest in recent years as versatile substrate for the design of nanocatalytic model systems. In particular, it has been proposed theoretically and confirmed experimentally that the electronic structure of adsorbates can be influenced by the layer thickness and the stoichiometry, i.e., the type and number of defects, of the oxide film. This has important consequences on the chemical reactivity of the oxide surface itself and of oxide supported metal clusters. It also opens new possibilities to influence and to control chemical reactions occurring at the surface of these systems. The present feature focuses on very recent experiments that illustrate the effects of a proper adjustment of layer thickness and composition of ultrathin MgO(100) films on chemical transformations. On the magnesia surface itself, the photodissociation dynamics of methyl iodide molecules is investigated via femtosecond-laser pump–probe mass spectrometry. Furthermore, the catalytic oxidation of

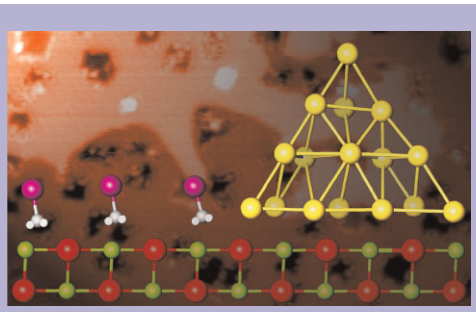

carbon monoxide at mass-selected Au_{20} clusters deposited on magnesia is explored through temperature programmed reaction measurements. In the latter case, detailed first principles calculations are able to correlate the experimentally observed reactivity with structural dimensionality changes that are induced by the changing thickness and composition of the magnesia support.

1 Introduction Oxide surfaces play an important role as active substrates as well as metal cluster support for various applications in surface chemistry and catalysis [1–3]. The molecular level perception of oxide surfaces greatly benefited from the preparation of well-defined oxide films of only a few atomic layers thickness on metal single crystal substrates [4, 5]. Such ultrathin oxide films allow the application of advanced surface science analytical techniques, in particular those relying on charged species, because measurement difficulties related to surface charging are circumvented due to the ultrathin nature of the oxide films. Nevertheless, already oxide films with a thickness of only about five atomic layers commonly exhibit structural and electronic properties that largely resemble those of the bulk oxide materials [6–8]. It has been recognized on the other hand that single crystal metal supports may strongly influence the chemical and physical properties of supported oxide films, when the film thickness is below five layers [6, 9–14]. In this respect, particular attention has been paid recently to adsorbate charging phenomena [12, 15] that occur, if molecules or metals with high electron affinity interact with low work function ultrathin oxide film substrates. The charging is generally believed to occur due to direct electron tunneling through the ultrathin film, if the

insulating layer is less than about five monolayers thick [8, 12, 15, 16]. Interesting consequences of such charging on, e.g., the adsorbate-surface bonding and the adsorbate structure have been predicted theoretically [12, 14, 16, 17] and also demonstrated experimentally [18]. The predicted changes of the *chemical* properties of these oxide films at the ultrathin limit [7] and of metal clusters deposited on such films [14] have also been impressively confirmed in recent experiments [9] and we aim to highlight this aspect of chemical reactivity here.

This feature article presents snapshots of the current state of research which is concerned with the possibility to influence and to control reaction dynamics and heterogeneous catalytic chemistry occurring on magnesia ultrathin films and on magnesia supported gold clusters through variation of film thickness and defect structure of the film.

In the following section we will first briefly review the preparation and characterization of ultrathin magnesia films on Mo(100). Subsequently, experimental evidence for a thickness dependent work function variation will be discussed and the generation of surface defects as well as their characterization will be presented. In Section 3, the dissociation dynamics of the prototypical photochemical model molecule methyl iodide on the surface of a magnesia ultrathin film will be discussed with an emphasis on the influence of oxide layer thickness and defect structure on the experimentally observed femtosecond (fs) time-resolved dynamics. Finally, Section 4 will be concerned with the effect of these parameters on the oxidation of carbon monoxide at the nanocatalytic model system Au_{20} on MgO/Mo(100) demonstrating the tunability of catalytic reactivity by exploiting substrate-induced structure–reactivity relationships.

2 Magnesia ultrathin films

The most widely investigated surface of magnesia is MgO(100). Ultrathin films with this surface orientation are most commonly epitaxially grown on Ag(100) or on Mo(100) single crystal substrates [5]. The silver surface presents the best matching lattice constant (3% mismatch as opposed to 5% for molybdenum) [6, 19, 20], yet molybdenum has been chosen as a substrate in the experiments presented below because of its high melting point as a refractory metal enabling facile high temperature treatment [11, 21–27].

2.1 Preparation and characterization

The MgO ultrathin films employed in the investigations presented below were prepared, in accordance with the general procedure reported in the literature, by evaporation of magnesium metal in an atmosphere of $2–5 \times 10^{-7}$ mbar of oxygen [21, 22, 24]. The preceding cleaning procedure of the molybdenum crystal consisted in an initial heating to 1200 K in 2×10^{-7} mbar of oxygen and subsequent flash to 2000 K. During the deposition, the Mo(100) crystal was held at 300–600 K. The Mg evaporation rate (typically 0.15 ML/min or larger) was determined by temperature programmed desorption (TPD) and Auger electron spectroscopy (AES) investigation of Mg layers deposited directly onto the Mo(100) surface. Gradual increase of the magnesium quantity on the molybdenum surface leads to a break-point in the intensity ratio of the $Mg(L_{23}VV)$ AES signal at 44 eV (or the $Mg(KL_2L_3)$ signal at 1174 eV) to the Mo(MNN) AES signal at 186 eV, which coincides with the appearance of the multilayer peak in the TPD spectra and corresponds to the exact amount of Mg needed for completion of the first Mg layer on Mo(100). The number of Mg atoms in the first monolayer of MgO(100) is identical to this amount [22].

MgO grows in orientation (100) on Mo(100), rotated by 45° with respect to the substrate [22]. Accurate control of the film thickness can be achieved through variation of the growth time. The physical properties of the films and of the underlying crystal, i.e., the electronic and geometric structure as well as the composition, were characterized by AES, metastable impact electron spectroscopy (MIES), ultraviolet photoemission spectroscopy (UPS), fs-laser photoemission spectroscopy, low energy electron diffraction (LEED), and electron energy loss spectroscopy (EELS) in the presented experiments [9, 11].

The MgO films present long-term stability and do not decompose at temperatures up to 1100 K [21]. Under these conditions, the concentration of point defects on the surface of magnesia films prepared as described above is very low [28, 29] (see also Section 2.3).

2.2 Coverage dependent work function

For a given metal or molecular adsorbate the electronic interaction with the oxide film is largely determined by the surface work function of the substrate [16]. In the case of ionic oxides like MgO, the oxide thin film induces a substantial reduction of the work function of the underlying metal single crystal surface. Theoretical considerations proposed this work function reduction to be strongly dependent on the type of metal underneath the oxide film as well as on the oxide layer thickness in the range of up to three monolayers [10, 30]. The resulting charge transfer through the oxide ultrathin film was predicted to have important consequences on the adsorbate reactivity [14]. These predictions and concurrent experimental evidence for adsorbate charging has led to the advertisement of ''metal-supported ultrathin oxide films as designable catalysts and catalyst supports'' [31].

Nevertheless, until very recently, neither experimental surface work function measurements nor direct experimental evidence for a layer thickness dependent chemical reactivity were available for ultrathin oxide films. In this section we will discuss the now existing work function measurements as a function of the MgO film thickness [11, 13, 32] before presenting two layer thickness dependent reactivity studies in Sections 3 and 4.

In one experiment fs-laser photoemission spectroscopy was applied to obtain information about the integral work function Φ of Mo(100) covered by stoichiometric magnesia layers of different thickness [11]. The relative changes of the surface work function, $\Delta\Phi$, as a function of the MgO layer thickness, Θ, that have been obtained from fs-laser

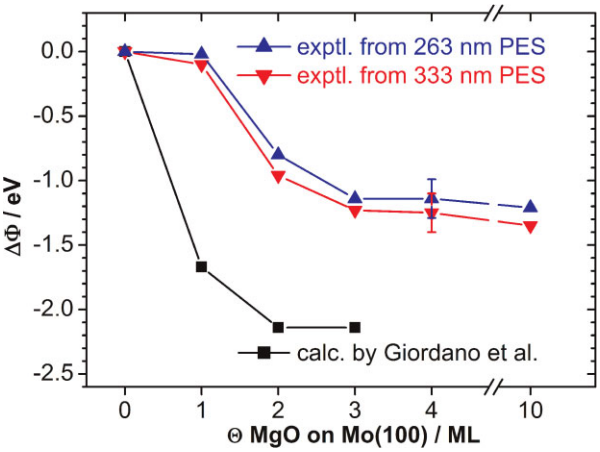

Figure 1 (online colour at: www.pss-b.com) Change of the electronic work function $\Delta\Phi$ of the Mo(100) surface as a function of the number of MgO(100) overlayers Θ as determined by fs-laser photoemission spectroscopy (PES). The experimental data obtained with 263 nm (blue triangles) and 333 nm (red upside-down triangles) excitation wavelength, respectively, are compared to calculated values reported in Ref. [10] (black squares). Reprinted from Ref. [11] with permission of The American Chemical Society.

photoemission spectra are plotted in Fig. 1 together with the theoretically predicted values from the work of Pacchioni and coworkers [10]. Comparable data have been obtained recently for MgO(100) on Ag(100) with Kelvin probe force microscopy (KPFM) [13].

The theoretical calculations predict that Φ decreases for the first two monolayers of MgO on Mo(100) and remains constant afterward. The experimental fs photoemission results confirm the rapid decrease of Φ with the deposition of the first few monolayers (cf. Fig. 1). However, in the experiment, Φ decreases up to an MgO film thickness of 3 ML by only about 1.3 eV compared to the bare Mo(100) surface and remains constant afterward. Furthermore, the very first magnesia ML changes Φ only slightly in the experiment, in contrast to the theoretical prediction. This discrepancy in the influence of the first MgO monolayer on the electronic structure of the surface has been explained by an imperfect geometric arrangement of the very first layer in the experiment. Previous LEED and scanning tunneling microscopy (STM) investigations of MgO(100) on Mo(100) indicate that after deposition of approximately one monolayer, the film still exhibits large holes, confined by nonpolar [100] and polar [110] oriented edges [22, 26]. The incompleteness of the first monolayer (90% fractional coverage) governed by areas with 2 ML thickness has also been observed for MgO on Ag(100) [33]. After deposition of the amount of MgO corresponding to nominal 2 ML, the metal surface is completely covered with magnesia [6, 26] and exhibits a distinct moiré-type superperiodic structure [26, 33]. At even larger coverages (>5–7 ML), the formation of a mosaic structure has been observed that is spanned between a dislocation network which relaxes the strain in the oxide layer (due to the 5% lattice mismatch between Mo(100) and MgO(100)). A mean domain size of 55 Å has been reported for the mosaic structure [26, 27, 33]. A similar mosaic pattern had also been observed for MgO grown on Ag(100) (3% lattice misfit) [34]. Above 7 ML film thickness, the oxide was found to gradually flatten and the global roughness to decrease, indicating a flat and defect-poor surface structure [26].

Coverage dependent photoemission spectroscopy employing ultraviolet radiation (UPS) has also been applied to MgO on an Fe(100) surface [35]. In these experiments, very little modification was seen in the emission close to the Fermi energy (between 0 and 3.5 eV electron binding energy) for low coverages of 0.5, 1, and 2 ML MgO. The major modification at these coverages consisted in the appearance of an intense emission centered at approximately 5.5 eV, which is characteristic of highly hybridized O 2p and Mg 3s valence band states of the MgO film.

While photoemission spectroscopy only yields information about the integral surface work function, KPFM is able to measure the local work function with a lateral resolution at the nanometer length scale. In KPFM, the Kelvin modulation technique is integrated into noncontact atomic force microscopy (nc-AFM) in that a topography image and an image of the local surface work function are obtained at the same time [36]. KPFM on single crystal magnesia surfaces, for instance, show work function changes of up to 1.5 eV for low-coordinated surface sites like steps, kinks, and corners, which were tentatively assigned to negative and sometimes to positive defects like F centers on the MgO(001) surface [37].

The images in Fig. 2 show characteristic details, which appear during KPFM imaging of MgO(100) islands of one layer height on Ag(100) [32]. From the topography image in Fig. 2a it can be seen that the lateral contrast strongly depends on the tip conditions. The major tip change that occurred during image acquisition (as indicated by the arrow in Fig. 2) even lead to a complete contrast inversion in the AFM micrograph (dark MgO islands in the bottom part, bright MgO islands in the top part of Fig. 2a).

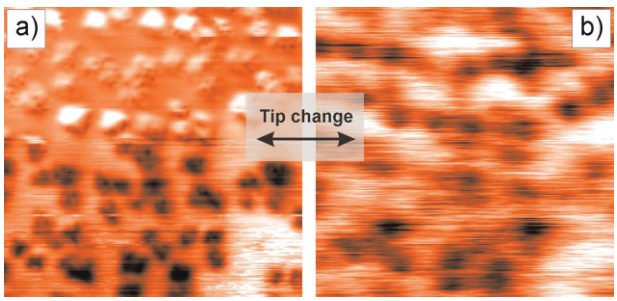

Figure 2 (online colour at: www.pss-b.com) Micrographs ($92 \times 92\ nm^2$) showing (a) the topographic nc-AFM image and (b) the KPFM image obtained in the same measurement from MgO islands on Ag(100). The MgO island size is about $10 \times 10\ nm^2$. Several changes in the tip conditions occurred during data acquisition as indicated by the arrows in the images [32]. A mean subtraction routine was applied for both images in order to show maximal lateral contrast.

In contrast, the MgO islands were always recorded with dark contrast in the Kelvin image in Fig. 2b, independently of the tip changes. A darker contrast in KPFM micrographs corresponds to a smaller work function of the considered surface position [38]. An analysis of the Kelvin image yielded an average value of $\Delta\Phi$ between -0.15 and -0.3 eV. This is less than expected from theoretical considerations which give $\Delta\Phi = -0.7$ to -1.0 eV [10, 30] but also in comparison to recently obtained values by KPFM [32]. The discrepancy between experiment and theory is due to the fact that the islands imaged with KPFM were smaller than the microscope probe tip apex. Because of the long-range character of the tip–surface electrostatic interaction, the measurements sample not only the MgO island but rather integrate over the 1 ML islands and parts of the silver surface in the vicinity [32].

2.3 Preparation of defective magnesia films The MgO(100) surface is inert, irreducible, nonpolar, and easy to prepare. However, this surface becomes chemically reactive once defects are formed [1]. Several procedures to create surface defects on magnesia thin films have been described in the literature: Electron bombardment [20, 28, 39, 40], thermal treatment [28, 41, 42], Ar^+ bombardment [28, 43], addition of Li atoms [42], and deposition of Mg after preparation [43]. Defect-rich magnesia surfaces are also generated, if the magnesium metal evaporation rate is very fast during the growth process of the MgO films so that not all Mg surface atoms are fully oxidized [44, 45].

Surface defects are represented by, e.g., step edges, kinks, and atom vacancies. The oxygen vacancies (F centers) are responsible for the reactive character of the magnesia surface [46]. When an oxygen atom has left the magnesia surface, electrons can be trapped in the vacancy. Depending on the resulting charge, the vacancy is termed F, F^+, or F^{2+} corresponding to the removal of a neutral O atom, of an O^-, or of an O^{2-} anion, respectively [47]. Theoretical calculations indicate that the F centers at low coordinated sites are more stable than at high coordinated sites [47]. This is directly connected to the energy required to remove an oxygen atom from magnesia. Therefore, F centers located at corners are more stable than at steps. The stability decreases further for vacancies on surface terraces and the most unstable F centers are located in the bulk. This trend is also valid for F^+ centers. In contrast, the low and high coordinated F^{2+} centers have comparable stabilities [47].

Experimentally, various analytical methods have been employed to investigate the F centers on magnesia ultrathin films like, e.g., EELS [42], electron spin resonance [40, 45, 48], scanning tunneling microscopy and spectroscopy [20, 48], as well as infrared vibrational spectroscopy [44, 45] and TPD [28, 44, 45] of adsorbed molecules like, e.g., NO. In addition, there is an extensive theoretical literature available on various aspects of defects in magnesia ultrathin films [8, 46, 49].

In the experiments presented in this report two different methods have been employed for the generation of defective magnesia surfaces. (i) Thermal annealing close to the decomposition temperature of magnesia has been employed to investigate the adsorption and photoreaction dynamics of molecular adsorbates. (ii) Control of the surface defect concentration through variation of the Mg evaporation rate during film preparation has been applied to study the adsorption and catalytic properties of Au_{20} clusters.

The thermal annealing procedure (i) consists in fast heating of the sample to 1000 K with a rate of up to 5 K/s and a subsequent slow further temperature increase to about 1200 K with a rate of 0.3–0.5 K/s. It was observed that a fast annealing (5 K/s) directly to 1200 K lead to noncontrollable preparation of the samples, due to the desorption of a significant part of the magnesia film as evidenced by post-annealing AES measurements.

To illustrate the geometric thin film structure obtained by the annealing procedure, Fig. 3 shows the LEED patterns of the Mo(100) substrate and of a 10 ML MgO film grown on Mo(100) before and after annealing at 1200 K. Initially, the clean Mo(100) surface presents a sharp (1×1) LEED pattern (Fig. 3a). After the deposition of 10 ML MgO the diffraction pattern is not changed, which reflects the epitaxial growth of the oxide film, but the LEED spots becomes broader (Fig. 3b). A change appears in the LEED pattern when the magnesia films are annealed at temperatures around 1200 K (cf. Fig. 3c and d). The LEED spots split and distinct crosses around each fundamental spot oriented along the [110] direction appear. This observation is in agreement with previous reports [25–27]. Similar results have also been

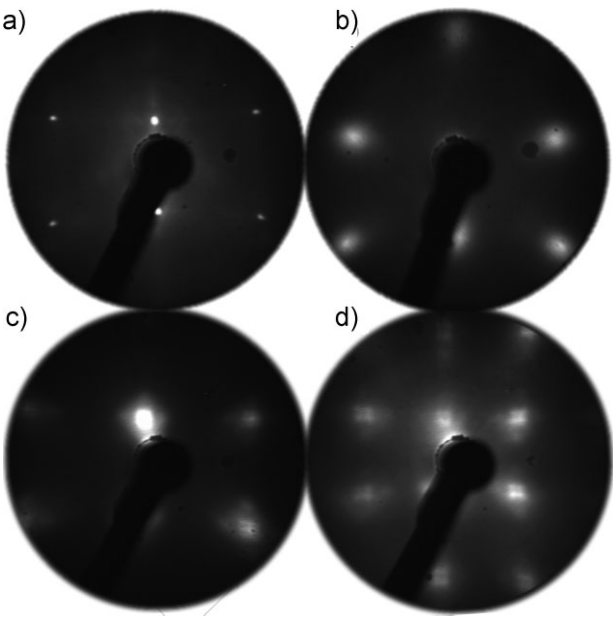

Figure 3 LEED images recorded from (a) the Mo(100) substrate (primary electron energy, $E_p = 78$ eV); (b) a 10 ML MgO film on Mo(100) as prepared (see text for details, $E_p = 78$ eV); (c) a 10 ML MgO film on Mo(100) after annealing at 1210 K ($E_p = 78$ eV); and (d) the same MgO film but with $E_p = 150$ eV.

reported for magnesia films grown on Fe(100) [50] and Ag(100) single crystal surfaces [34, 51] and were attributed to the formation of a mosaic structure spanned between a dislocation network that relaxes the strain in the oxide layer. The size of the LEED spot crosses depends on the inclination angle of the tilted regions [26].

Yan et al. [41] determined the relative concentration of the F centers created by the annealing procedure on the magnesia surface by means of high resolution EELS (HREELS). No defects are created up to about 1070 K. Subsequently, the density of F centers increases with increasing annealing temperature as can be seen from Fig. 4.

The second method to prepare defect-rich MgO films (ii) employed in the experiments presented here relies on the observation that the Mg evaporation rate during thin film preparation determines the defect density. Films prepared at low evaporation rate ($\sim$0.15 ML/min in 5×10^{-7} mbar O_2 environment) are essentially free of point defects like oxygen vacancies and are termed "defect-poor" in the following. In contrast, magnesia films prepared at higher evaporation rates ($\sim$1.5 ML/min in 5×10^{-7} mbar O_2 environment) exhibit a considerable concentration of oxygen vacancies as evidenced by MIES and are denoted defect-rich films [9].

For oxide materials the MIES spectra provide direct information about the electronic density of states at the surface. Defect-poor films prepared at low Mg evaporation rate exhibit MIES spectra (Fig. 5a and b) that point toward the absence of electronic states in the band gap of MgO and particularly to the absence of F centers. F centers manifest themselves by a MIES contribution at binding energies peaked at around 2.2 eV. Such a MIES contribution peaked at around 2 eV is clearly observed in the case of defect-rich films (spectrum (c) in the inset of Fig. 5). This proves that F centers are indeed present on defect-rich films (cf. also Ref. [28]). The F centers are oxidized when exposing the films to oxygen at high temperatures as illustrated by the MIES spectrum (d) shown in the inset of Fig. 5.

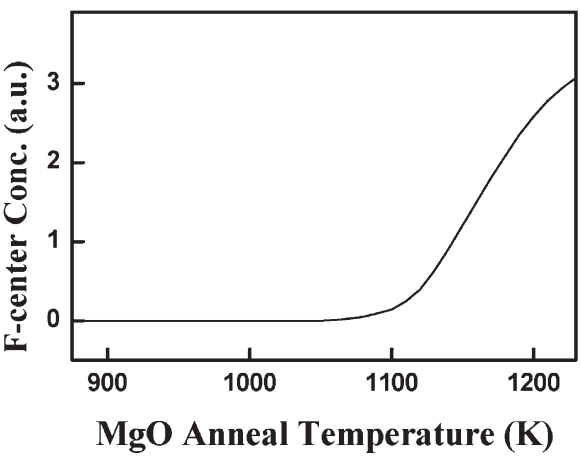

Figure 4 The relative concentration of F centers in MgO(100) films on Mo(100) as a function of the annealing temperature as determined by EELS. Reprinted from Ref. [41] with permission of The American Chemical Society.

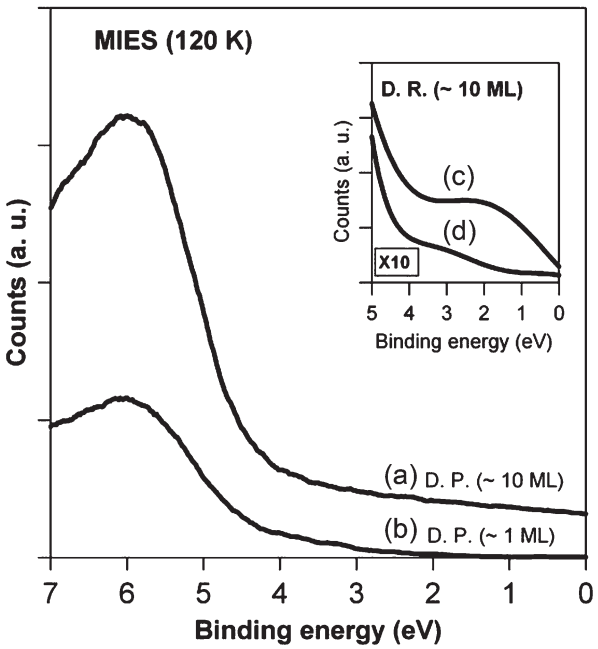

Figure 5 MIES spectra taken from (a) a thick defect-poor (D.P.) and (b) a thin defect-poor film. The inset depicts the MIES spectra of (c) a thick ($\sim$10 ML) defect-rich (D.R.) film and (d) the same film after annealing in oxygen. Note the MIES contribution peaked at $\sim$2 eV in spectrum (c) which originates from F centers. Reprinted from Ref. [9] with permission of The American Chemical Society.

3 Molecular photoreaction dynamics on magnesia thin films In order to study the molecular photoreaction dynamics at the oxide film surface, a recently developed technique which combines fs-laser pump–probe spectroscopy with multiphoton ionization time-of-flight mass spectrometry was employed [52, 53].

As a model system methyl iodide adsorbed at submonolayer coverage on the ultrathin magnesia films was chosen. The photodissociation of methyl iodide through electronic excitation to the A-band has been extensively studied in the gas phase, mostly in the frequency (e.g., see Ref. [54] and references therein), but also in the time domain [55–57]. A great deal of theoretical contributions as well have been published due to the fact that methyl iodide represents a benchmark system for calculations on the fragmentation of a small polyatomic molecule in two electronic states (e.g., see Refs. [58, 59] and references therein).

Magnesium oxide was chosen as a substrate because it is transparent in the wavelength region of the methyl iodide A-band. In addition, photofragmentation of methyl iodide molecules adsorbed on a magnesia single crystal surface has been investigated in detail experimentally [60] as well as theoretically [61, 62].

The excitation of the methyl iodide to the dissociative A-band was performed with the fs pump laser pulses tuned to a wavelength of 266 nm. At this wavelength, the methyl iodide dissociation involves primarily two repulsive excited

electronic states denoted as $^3Q_{0+}$ and $^1Q_1$ by Mulliken [63]. These states lead to methyl fragments and iodine atoms in the ground (I) and the spin–orbit excited state (I^*), respectively. The detection of the reaction products was accomplished with the probe pulses tuned to a center wavelength of 333.4 nm. The wavelength of the probe pulse was chosen in order to sensitively detect the methyl fragments through (2 + 1) REMPI via the $3p^2A_2'$ Rydberg state [64].

After ionization, the reaction products were instantaneously removed from the surface by a static electric field which also constituted the first acceleration field of the time-of-flight mass analyzer. The pump–probe schema and the relevant potential energy curves of the methyl iodide ground state and the electronically excited A-band are depicted in Fig. 6. As the exact influence of the surface on the methyl iodide potentials is not known and because the methyl iodide molecules do only weakly bind to the magnesia surface [62], the shown gas phase potentials are assumed to be almost unperturbed by the defect-free surface to a first approximation.

3.1 Photodissociation of methyl iodide on the MgO surface Fs time-resolved transients were obtained by monitoring the methyl signal intensity after photodissociation of CH_3I or CD_3I, respectively, adsorbed on MgO/Mo(100) at sub-monolayer coverage. Figure 7a shows the result for CH_3I molecules on 10 ML MgO/Mo(100) measured with a probe laser power of 70 mW/cm^2. The transient signal exhibits a steep rise starting at zero delay time with a maximum reached around 130 fs. It subsequently decays but does not reach the initial value measured at negative delay times again. Instead, a small but clearly apparent offset is observed which stays constant at longer positive delay times. Fitting of an exponential "rise and decay" model (peak with subsequent offset) to the experimental data gave similar time constants of $\tau_1 = \tau_2 = 90$ fs for the rise and the decay component of the observed peak, respectively. The transient signal obtained for CD_3I at

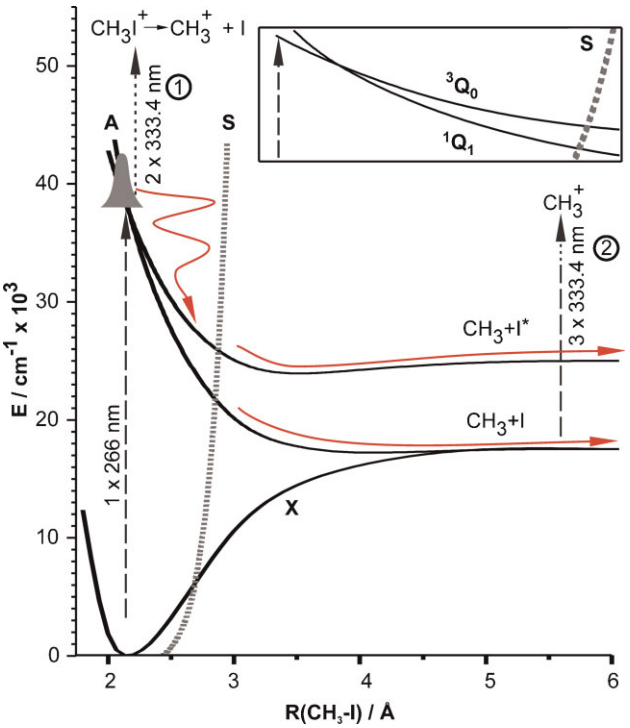

Figure 6 (online colour at: www.pss-b.com) Potential energy diagram of free methyl iodide [58, 79]. The solid arrows illustrate the propagation of the wavepacket. The dashed arrows represent the laser excitation and the two detection schemes (1) and (2). The detection energies are not drawn to scale. The potential S reflects the Lennard–Jones interaction between the methyl group and the magnesia surface [65]. The inset shows a magnification of the methyl iodide A-band excitation region.

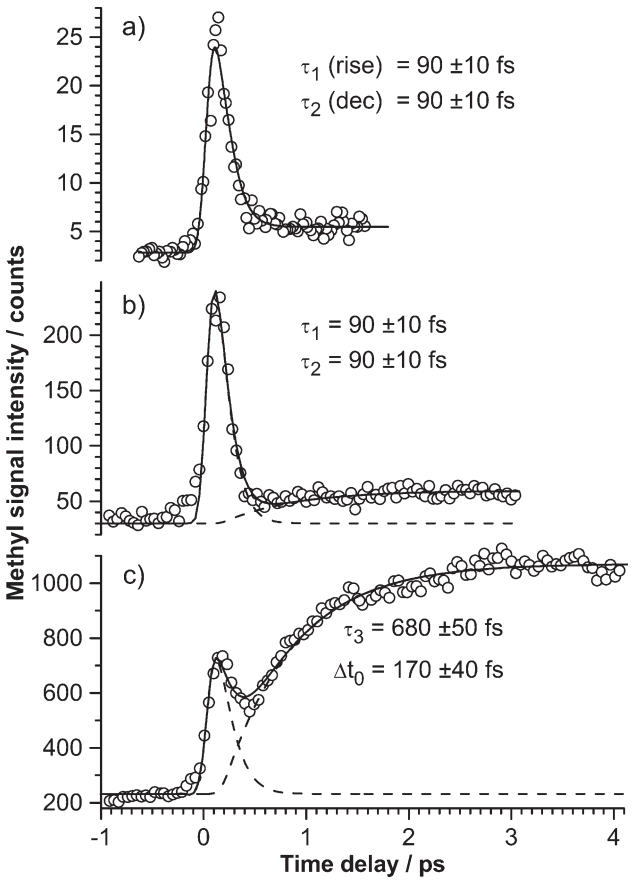

Figure 7 Fs transients of the photodissociation of 0.25 ML methyl iodide on 10 ML MgO/Mo(100) obtained by monitoring the methyl cation signal as a function of the pump (dissociation)–probe (ionization) delay time (surface temperature: 90 K). (a) CH_3I transient measured with 1 mW/cm^2 pump and 70 mW/cm^2 probe laser power. (b) CD_3I transient measured with comparable laser conditions (pump: 2 mW/cm^2; probe: 70 mW/cm^2). (c) CD_3I transient obtained with 600 mW/cm^2 probe laser power (pump power: 2 mW/cm^2). The solid line has been obtained by fitting a peak with exponential growth model (convoluted with the pump–probe crosscorrelation function) to the experimental data yielding the indicated time constants for peak rise (τ_1), peak decay (τ_2), and exponential growth (τ_3, with initial delay time Δt_0). The dashed curves represent the separated peak and exponential growth components of the fit. Reprinted from Ref. [52] with permission of The American Physical Society.

comparable laser conditions is displayed in Fig. 7b. The appearance is basically identical to the CH_3I signal in Fig. 7a with similar time constants.

Figure 7c shows the transient CD_3^+ signal recorded with the average probe power increased to 600 mW/cm^2. While the peak structure at short delay times is still present, the offset at longer delay times is now considerably enhanced and exhibits an exponential rise. Detailed probe pulse power dependent measurements of this latter rising signal supports its attribution to the resonant ionization ((2 + 1)-REMPI) of neutral methyl fragments resulting from the A-band dissociation. For the exponential growth at longer delay times a time constant of $\tau_3 = 680$ fs with an initial delay time of $\Delta t_0 = 170$ fs was obtained from the fitting procedure [52].

The proposed excitation and detection (ionization) pathways that lead to the observed transient methyl signal are illustrated schematically in Fig. 6. Due to single photon 266 nm excitation to the dissociative A-band a wavepacket is created (almost exclusively on the $^3Q_{0+}$ state) that subsequently propagates on the repulsive potential curve leading to methyl and I* fragments. Because of a conical intersection between the $^3Q_{0+}$ and the $^1Q_1$ states a bifurcation of the wavepacket is possible resulting in methyl and ground state I fragments (see inset in Fig. 6).

The peak structure at early delay times in the transients in Fig. 7 was attributed to the dynamics of the dissociating excited transition state of methyl iodide on the A-band states, $CH_3I^{*\ddagger}$, which is directly ionized by the probe pulse briefly after A-band excitation. Subsequently, rapid decomposition of the CH_3I^{+*} ion leads to the observed ionized fragments (detection path (1) in Fig. 6) according to:

$$CH_3I_{ads} \xrightarrow{266\ nm} CH_3I^{*\ddagger}{}_{ads} \xrightarrow{2\times 333.4\ nm} CH_3I^{+*} \rightarrow CH_3^+ + I \quad (1)$$

The exponential rise of the transient signal after a few hundred femtoseconds could be assigned to the direct (2 + 1)-REMPI detection of the emerging neutral methyl fragment (detection path (2) in Fig. 6):

$$CH_3I_{ads} \xrightarrow{266\ nm} CH_3I^{*\ddagger}{}_{ads} \rightarrow CH_3 + I/I^* \xrightarrow{(2+1)\times 333.4\ nm} CH_3^+ + I/I^* \quad (2)$$

The initial time delay of the exponential growth part of the methyl signal ($\Delta t_0 = 170$ fs; cf. Fig. 7c) reflects the liberation of the methyl fragments from the molecular force field and from the force field of the magnesia surface. Gas phase investigations of the A-band dissociation of isolated methyl iodide molecules showed a 120 fs coherent delay in the methyl fragment emergence followed by an instantaneous signal appearance [57]. Because of the considerably prolonged delay and the 680 fs rise time observed here, the direct ejection of methyl as in the free molecule can be ruled out. Instead, the data favor a CH_3I adsorption structure with the methyl facing the magnesia substrate.

This adsorption picture is in accordance with the extended transition state lifetime observed here (peak structure centered at about 130 fs in Fig. 7, cf. Eq. 1) compared to the free molecule dissociation (transition state lifetime <50 fs [56]).

The extended time needed for the liberation of the methyl thus reveals the effect of the magnesia surface that manifests itself in the trapping of the $CH_3I^{*\ddagger}$ transition state. The subsequent growth of the methyl signal with a time constant of $\tau_3 = 680$ fs (Fig. 7c) is consequently interpreted as the average lifetime of all trajectories leading from the transition state to the release of the methyl fragment. This corresponds to a temporal spreading of the initially prepared wavepacket due to the inelastic interaction with the substrate. The corresponding trajectories therefore include the motion of methyl toward the surface leading to the inelastic collision and the recoil away from the surface followed potentially by a collision with the slowly moving, heavy iodine atom. This interaction with both, the surface and the iodine atom, was predicted theoretically and was termed ''chattering'' motion [61, 62]. The scenario might proceed until the methyl trajectory is rotated away from the iodine trajectory far enough so that the fragment can escape. The dashed potential labeled S in Fig. 6 illustrates the Lennard–Jones-type interaction between the methyl group and the magnesia surface [65].

3.2 Photodissociation of methyl iodide on MgO films of variable thickness Figure 8 shows methyl signal transients obtained from sub-monolayer coverages of CD_3I adsorbed on the bare Mo(100) surface and from 1 to 6 ML thick MgO(100) films on Mo(100). On the Mo(100) surface the CD_3^+ transient signal does not exhibit an exponential growth part under any pump or probe laser conditions. It just consists of a peak structure centered at 58 ± 10 fs. According to the discussion in the preceding section, the peak signal can be assigned to the detection of the dissociating transition state of the excited methyl iodide molecules according to Eq. (1) (cf. also detection path (1) in Fig. 6). If this applies also to the methyl iodide molecules adsorbed on molybdenum, then the shift of the peak maximum to earlier times confirms a different interaction of the CD_3I molecules with the metal surface compared to the MgO film. In addition, it might indicate a different adsorption geometry that enables a faster release of the methyl fragments like, e.g., the iodine atom facing the molybdenum substrate. A halogen-down adsorption geometry is commonly observed for methyl halide adsorption on metal surfaces [66].

On a 1 ML thick magnesia film on Mo(100) the peak structure shifts to longer pump–probe delay times. Moreover, a small offset appears in the methyl signal at longer delay times. A further shift of the peak and an increase of the methyl offset signal is observed on 2 ML MgO. As apparent from Fig. 8, for magnesia films with 3–6 ML thickness no significant change of the transient signals is detected and the signal agrees well with the one recorded under similar laser conditions on a 10 ML MgO film (see Fig. 7a and b). Figure 9 summarizes the observed shift of the

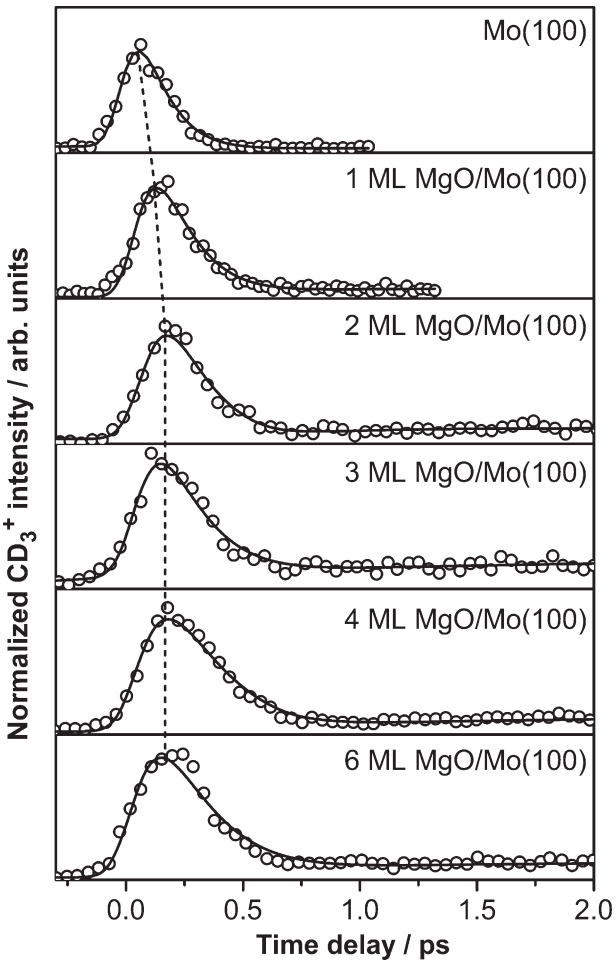

Figure 8 Time-resolved dissociation dynamics of CD_3I (0.25 ML) adsorbed on Mo(100) and on MgO films of variable thickness on Mo(100). The transients were obtained with 1 mW/cm^2 pump (266 nm) and 70 mW/cm^2 probe (333.4 nm) laser power. The solid line represents the fit of a peak model (with offset at long-delay times) to the experimental data. The dashed line indicates the shift of the peak maximum and has been drawn to guide the eye.

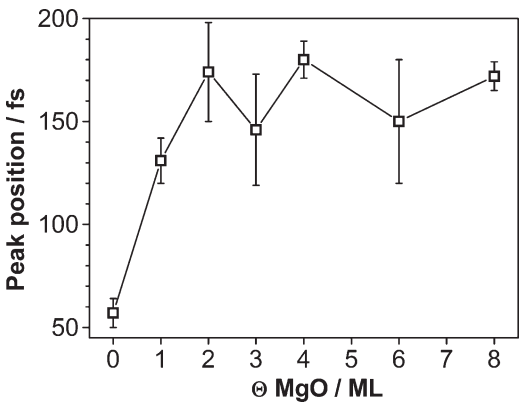

Figure 9 Position of the peak maximum in the methyl transient data in Fig. 8 as a function of the magnesia film thickness. The shown error bars result from the accuracy of the fitting procedure.

transient peak structure as a function of the magnesia coverage.

Clearly, except for 1 ML MgO/Mo(100), where the magnesia film does not yet completely cover the metal substrate (see Section 2.2), the layer thickness does not notably influence the observed reaction dynamics. However, the dynamics resulting from electronic excitation and subsequent multiphoton ionization should be extremely sensitive to changes in the electronic level structure of the adsorbed molecules. Thus, it can be concluded that in the case of CD_3I on magnesia ultrathin films, electronic coupling of the molecules to the underlying molybdenum substrate leading, e.g., to charging effects, should only play a minor role. In this respect it would be very interesting to investigate the dissociation and desorption dynamics of adsorbate molecules with large electron affinity, like NO_2, for which a considerable charging at the ultrathin film surface has been predicted [16, 17].

3.3 Photodissociation of methyl iodide on defect-rich MgO films In contrast to the weak dependence of the photodissociation dynamics on the magnesia layer thickness, significant differences have been observed between "as prepared" (defect-poor) and defect-rich MgO films. In Fig. 10 TPD spectra recorded from 0.5 ML CD_3I on 10 ML MgO films on Mo(100) before and after annealing at 1200 K are presented (cf. also Section 2.3). Methyl iodide binds only weakly to the magnesia surface and desorbs without decomposition below 180 K [52, 67]. If methyl iodide is adsorbed on MgO films on which surface defects were generated through thermal annealing, two new distinct desorption features appear (see red spectrum in Fig. 10). First, a shoulder around 140 K, which extends up to 220 K, appears at the low temperature desorption peak that also exists on defect-poor films. Second, a weak separated desorption peak at 270 K is observed. These desorption characteristics do not change, if the annealing temperature is varied between 1180 and 1240 K as can be seen from the inset in Fig. 10. LEED and HREELS data presented in Section 2.3 indicated the presence of extended dislocation networks and of oxygen vacancy defects on the high temperature annealed magnesia thin films. Such defect structures present stronger binding sites to the CD_3I molecules which are likely responsible for the higher temperature desorption features in Fig. 10.

The femtosecond photodissociation dynamics of methyl iodide adsorbed at 90 K on a 10 ML MgO film that had been annealed at 1200 K is presented in Fig. 11. In contrast to the CD_3^+ transient signals measured from a defect-poor magnesia surface (Fig. 7), the peak structure at early pump–probe delay times is very weak in Fig. 11a compared to the exponential growth component at later delay times. Moreover, the intensity ratio of the peak structure to the exponential growth structure in the transient methyl signal was found to depend on the methyl iodide coverage (see Fig. 11). Such a coverage dependent variation of the peak structure intensity relative to the exponential growth

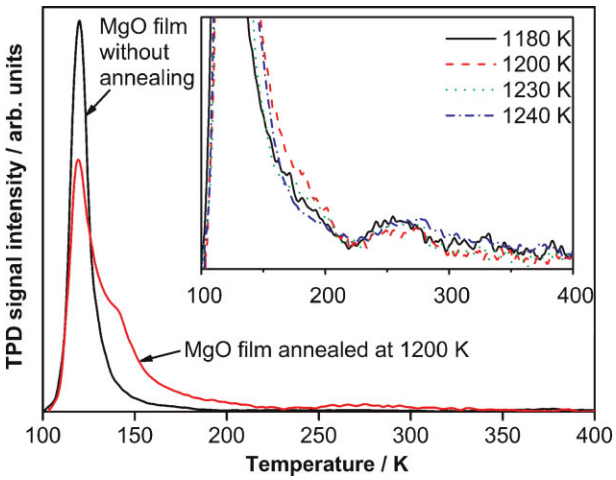

Figure 10 (online colour at: www.pss-b.com) TPD spectra of methyl iodide molecular desorption from 0.5 ML CD_3I on 10 ML MgO/Mo(100) surfaces before (black graph) and after (red graph) annealing at 1200 K. Inset: TPD spectra from surfaces annealed at different temperatures between 1080 and 1240 K.

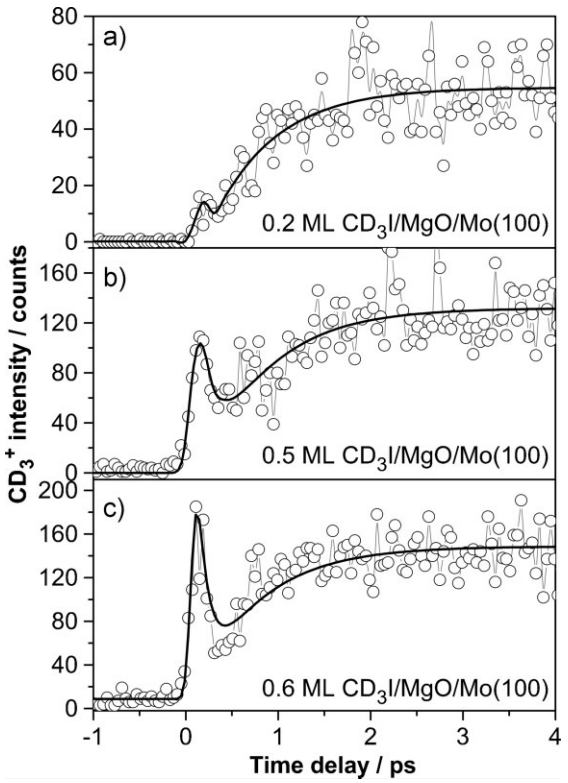

Figure 11 Fs time-resolved methyl signal emerging from the photodissociation of CD_3I on defect-rich, annealed 10 ML MgO on Mo(100). The CD_3I coverages increase from top to bottom: (a) 0.2 ML, (b) 0.5 ML, (c) 0.6 ML. The open circles represent the experimental data whereas the solid lines correspond to fits of a peak with delayed exponential rise model. Pump pulse: 266 nm, 2 mW/cm^2; probe pulse: 333.4 nm, 400 mW/cm^2.

component intensity and also to the total CD_3^+ transient signal has never been observed on defect-poor MgO/Mo(100) substrates.

Apparently, on the defect-rich, annealed MgO surface the detection of the methyl iodide transition state dynamics by means of one pump plus two probe photons (detection schema (1) in Fig. 6; cf. also Eq. 1) is suppressed, but the REMPI sampling of the emerging methyl fragments (detection schema (2) in Fig. 6; cf. Eq. 2) is not affected. A possible explanation might be the strong interaction between the adsorbed methyl iodide molecules and the surface defects which leads to a considerable distortion of the excited electronic states of methyl iodide rendering the detection via schema (1) in Fig. 6 unfavorable at the employed laser wavelength.

The observation that on the defect-rich, annealed magnesia films the peak structure in the transient methyl data at early delay times increases in relative intensity with the methyl iodide coverage (see Fig. 11), indicates that the molecules adsorb first at defect sites like steps, corners, and vacancies. At higher coverages also the defect-free areas of the magnesia surface become decorated and the resulting transient signal gradually starts to resemble the one obtained from the defect-poor surfaces (Fig. 7). Interestingly, the obtained time constants of the kinetic model do not differ significantly for the defect-poor and the defect-rich, annealed magnesia films.

As the methyl iodide molecules adsorbed on defect sites have higher desorption temperatures than molecules on the defect-free areas, transient CD_3 signals recorded at elevated surface temperatures should selectively reveal the dissociation dynamics of CD_3I on the defect sites. According to the TPD spectra of CD_3I on defect-rich, annealed magnesia films (cf. Fig. 10) the majority of CD_3I on defect-free areas should be desorbed at 150 K and the molecules remaining on the surface at higher temperatures are likely to be bound exclusively to defect sites. Figure 12 displays transient methyl fragment signals recorded at different surface temperatures on a defect-rich, annealed MgO film. Figure 12a shows the transient recorded at 90 K for reference. At a surface temperature of 160 K (Fig. 12b) the total signal intensity is considerably reduced. Nevertheless, it is quite apparent that the peak structure corresponding to the detection of the dissociative transition state is completely missing. At 250 K no signal is detected anymore, although the molecules corresponding to the 270 K TPD peak in Fig. 10 (red spectrum) should still remain on the surface. Possible reasons might be that the molecules cannot be excited at these adsorption sites or that the fragments are trapped at the surface and are not detectable with the employed probe laser wavelength.

4 Nanocatalytic properties of gold clusters on magnesia thin films The discovery that nanosize gold particles supported on metal oxide materials represent highly effective, selective, and energy efficient, i.e., low temperature, oxidation catalysts [68], has started a real "gold

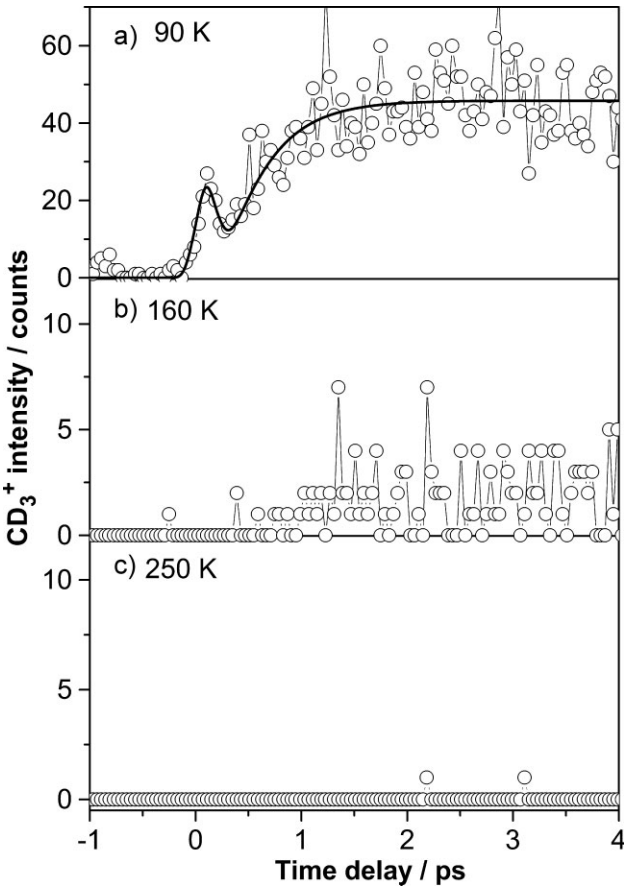

Figure 12 Fs time-resolved methyl signal emerging from the photodissociation of CD_3I on defect-rich, annealed 10 ML MgO on Mo(100) obtained at different temperatures: (a) 90 K, (b) 160 K, and (c) 250 K. The CD_3I coverage was 0.25 ML. The solid lines represent the fit of a peak with delayed exponential rise model to the experimental data.

rush'' [69] in catalysis at the end of the last century [70]. Among the numerous investigations aiming to reveal mechanistic details of the surprising activity of gold nanoparticles by employing surface science techniques and well-defined model catalysts [3, 71], in particular experiments with mass-selected gold clusters deposited on magnesia ultrathin films revealed striking and completely unexpected size dependent reactivities [72]. Hence, the exact atomically defined cluster size was identified as one key parameter to control the catalytic activity [73]. However, the experiments and especially concurrent theoretical simulations also pointed toward the importance of the support on the chemical reactivity. Oxygen vacancies interacting with the deposited gold clusters and leading to a charge transfer from the oxide film to the metal–adsorbate complexes were found essential for the activation of, e.g., molecular oxygen in the catalytic low temperature oxidation of CO [74].

Having identified the important role of charging to the catalytic activity of oxide supported gold nanocluster catalysts [72, 74], alternative ways to influence the electronic clusters–substrate interaction were envisaged. In particular, charging of gold atoms on less than 4 ML thin magnesia films, even in the absence of defect centers, has been predicted theoretically [15]. These findings were confirmed in STM experiments [18]. Subsequently, a charge transfer induced transition from 2D to 3D geometric structures was predicted for gold clusters containing 8, 16, and 20 atoms, when the oxide layer thickness was increased from below four to above five magnesia monolayers [12]. This was also confirmed in subsequent STM experiments [75]. Even the adsorption geometry of gold dimers on MgO(100) could be shown to sensitively depend on electronic charging phenomena [76].

Considerably less is known so far about the consequences of the substrate-induced effects on the chemical and catalytic properties of supported gold clusters. Landman and coworkers [14] predicted that the oxidation of CO catalyzed by gold nanoclusters would also proceed on a defect-free ultrathin magnesia film consisting of 2 ML of MgO supported on a metal (Mo(100)), and calculated the corresponding charge transfer induced 2D gold cluster geometries. Furthermore, a novel method for tuning the structure and catalytic activity of gold nanoclusters adsorbed on thin metal (Ag(100))-supported magnesia films, through the application of an electric field across the system, has been explored theoretically [77]. In the following we will review the first experimental report (accompanied by mechanistic *ab initio* simulations) on the control and manipulation of gold nanocluster catalysis through metal oxide support thickness and composition [9].

4.1 Influence of the layer thickness on the CO oxidation at magnesia supported Au_{20} clusters Au_{20} clusters were generated by a laser ablation source, mass separated with a quadrupole mass filter and soft-landed at 90 K onto the MgO/Mo(100) substrate with varying magnesia layer thickness. The cluster coverage was 0.005 ML or less ($1\,\text{ML} = 2.25 \times 10^{15}$ clusters/cm^2). These samples were exposed to one Langmuir of O_2 and ^{13}CO, each. The subsequently recorded temperature programmed reaction (TPR) spectra are displayed in Fig. 13 for the oxidized Mo surface, 1–3 ML thick MgO films, as well as for a 10 ML magnesia film on Mo(100).

No CO_2 formation is observed from Au_{20} clusters deposited on the bare Mo(100) surface which was previously exposed to oxygen at the same conditions as in a typical MgO film preparation step (Fig. 13a). If, however, MgO films with 1–3 ML thickness are employed as support for the gold clusters, two distinct CO_2 desorption peaks (at 180 K and at about 300 K) are observed in the TPR spectra of Fig. 13. In contrast, the TPR records for Au_{20} on a 10 ML magnesia film exhibit a single peak around 250 K.

This marked difference in the reaction temperature for less than 4 and 10 ML magnesia films is explained in terms of the electronic interaction of the gold clusters with the support and the consequences of this interaction on the geometric arrangement of the metal cluster. The most stable structure of Au_{20} on the 10 ML MgO films is a 3D tetrahedral geometry

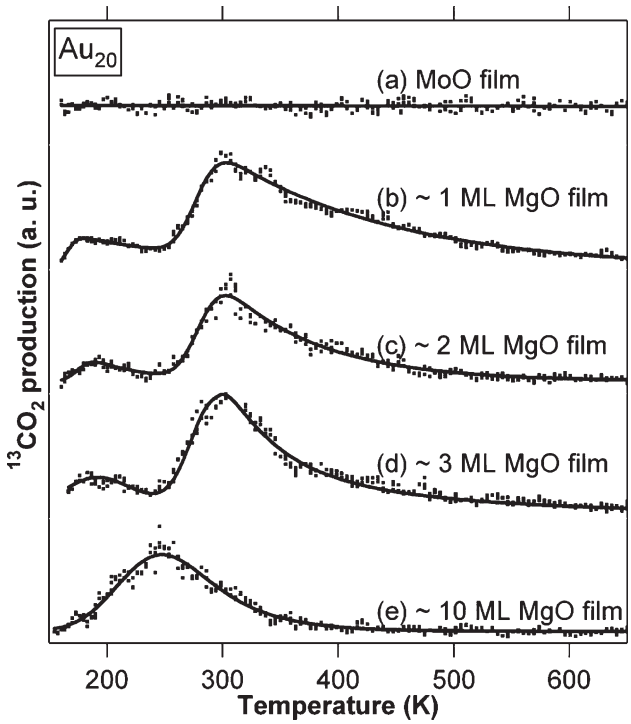

Figure 13 TPR spectra illustrating no activity of Au_{20} on (a) oxidized Mo, as well as the $^{13}CO_2$ formation from Au_{20} on (b) 1 ML, (c) 2 ML, (d) 3 ML, and (e) 10 ML MgO on Mo(100). Reprinted from Ref. [9] with permission of The American Chemical Society.

which is depicted in Fig. 14a. This structure is similar to the lowest energy isomer of free Au_{20} [78]. On only one to three monolayer thin magnesia films on Mo(100), a "wetting" planar (quasi-2D) island configuration as shown in Fig. 14b is energetically favorable instead. The origin of the planar geometry of the deposited gold clusters in this case is attributed to the attraction between the interfacial excess electronic charge and its image in the underlying substrate [9, 12].

Detailed *ab initio* simulations are able to assign distinct O_2 activation and CO oxidation mechanisms to the measured desorption peaks in Fig. 13 for the 10 ML as well as for the thin 1–3 ML magnesia films. One sequence of reaction configurations after oxygen activation that has been obtained for the planar configuration (Fig. 14b) is displayed in Fig. 15. This reaction path is able to account for the 180 K low temperature CO_2 formation peak in Fig. 13b to 13d [9] and involves the reaction of adsorbed CO with predissociated peripherally adsorbed O_2. When the surface-adsorbed CO reacts with an activated, but undissociated peripherally adsorbed O_2, a relatively high reaction barrier of 0.66 eV is found. Such a reaction path is predicted to contribute to the 300 K high temperature reaction channel observed experimentally (Fig. 13).

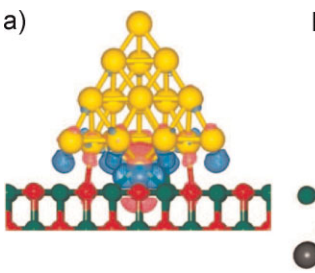

Figure 14 (online colour at: www.pss-b.com) Minimum-energy structures of Au_{20} clusters adsorbed on surfaces. (a) Tetrahedral Au_{20} cluster adsorbed on a thick MgO film (at the location of an F center). (b) Side view of a planar gold cluster adsorbed on a one-layer-thick MgO film supported on Mo(100). Superimposed on the atomic structures are density isosurfaces corresponding to the excess electronic charge distributions (blue corresponds to charge accumulation and pink signifies charge depletion with reference to the isolated cluster and surface components). Note the charge accumulation at the interfacial periphery regions. Color designation: Au atoms in yellow, O atoms in red, Mg atoms in green, and Mo atoms in black. Reprinted from Ref. [9] with permission of The American Chemical Society.

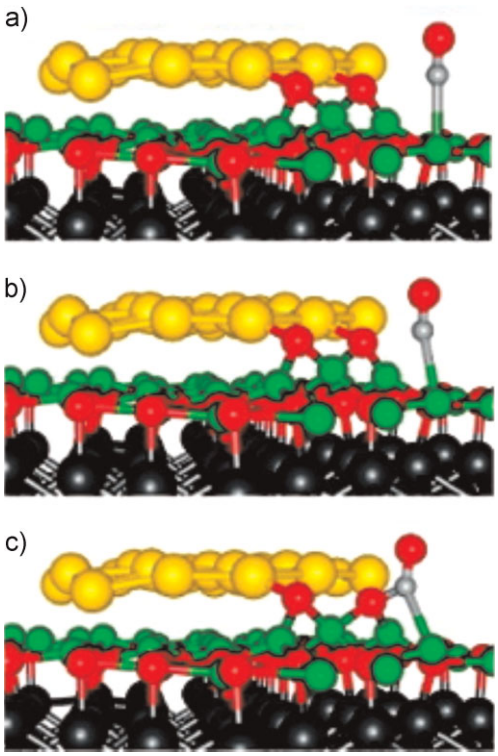

Figure 15 (online colour at: www.pss-b.com) Snapshots of a low temperature reaction pathway involving a planar Au_{20} on a one monolayer magnesia film on Mo(100). It starts from the adsorbed dissociated O_2 molecule (with a dissociation activation energy of 0.34 eV) and a CO molecule adsorbed on top of an Mg atom (E_B(CO) = 0.47 eV) shown in (a). The transition state geometry is depicted in (b). The generation of CO_2 entails a transition state barrier of 0.07 eV and a desorption energy of the product CO_2 (adsorption geometry shown in (c)) of 0.27 eV. Color designation: Au atoms in yellow, C atoms in grey, O atoms in red, Mg atoms in green, and Mo atoms in black. Reprinted from Ref. [9] with permission of The American Chemical Society.

Different geometrical configurations of Au_{20} on 1 ML MgO have been considered in the theoretical simulations as well, in order to obtain a comprehensive mechanistic picture of the layer thickness dependent catalytic activity [9].

4.2 CO oxidation at Au_{20} clusters supported on defect-rich magnesia films To investigate the influence of the film composition on the reactivity, TPR measurements were performed on 10 ML defect-rich magnesia films prepared as described in Section 2.3. The results are shown in Fig. 16b and compared to the TPR data from the 10 ML MgO defect-poor films (Fig. 16a, cf. also Fig. 13e). Unlike the low temperature reactivity of the defect-poor thick films (Fig. 16a) which apparently exhibits a single reaction channel, the TPR spectrum of Au_{20} on the defect-rich film (Fig. 16b) exhibits two reaction regimes (at 200 K and around 400 K).

The broad distribution of reactivity implicated by the two broad peaks in Fig. 16b can be correlated with the multiplicity of adsorbed cluster configurations that may coexist on such a defect-rich MgO substrate. These competing configurations differ from each other by the isomeric structure of the adsorbed nanocluster and the binding of the cluster to the surface. Two particular cluster structures, the tetrahedral geometry shown in Fig. 14a and a bilayer isomer, were assumed as starting geometries for the reaction path simulations [9]. Furthermore, the anchoring of the clusters to single or double (nearest-neighbor) surface oxygen vacancy defects was considered.

One selected CO oxidation pathway at a bilayer Au_{20} cluster bound to a surface oxygen vacancy is shown in Fig. 17 to illustrate one of the key concepts of nanocatalysis, namely, "dynamical structural fluctionality" [73]. This concept expresses the ability of the catalytic center (here the magnesia supported Au_{20} cluster) to change its atomic arrangement in the course of the reaction. It is exemplified by regarding the relative positions of the three Au atoms marked 1, 2, and 3 in the inset of Fig. 17a. In the initial minimum-energy configuration of the adsorbed reactants in Fig. 17a, the angle formed by the three marked Au atoms (with the atom marked 2 being at the apex of the triangle) takes the value $\theta(123) = 59^\circ$. As the transition state of the reaction pathway is approached (decreasing the distance between the C atom and the closest O atom of the adsorbed O_2 molecule) the above angle increases to a value of $\theta(123) = 76^\circ$ (Fig. 17b). The relaxed configuration in Fig. 17c is characterized by an angle $\theta(123) = 79^\circ$. Such fluctional structural variations serve to enhance the adsorption of the reactants and to lower the activation barriers for reactions between the adsorbed reactants. They are largest when both reactants adsorb on the metal cluster.

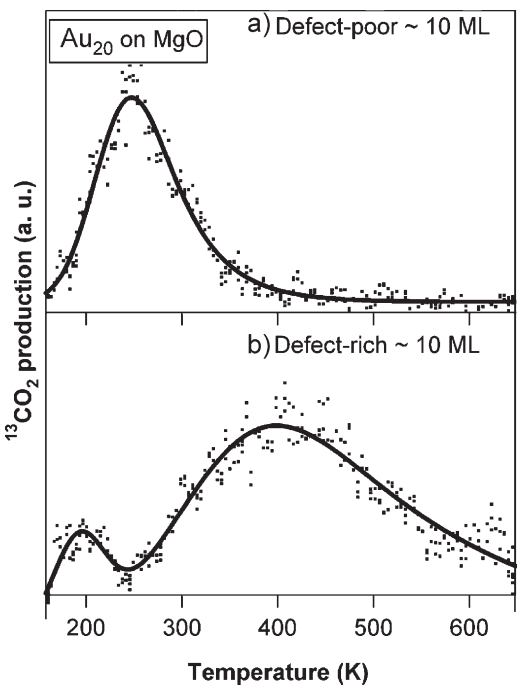

Figure 16 (a) TPR measurements obtained from the Au_{20}-based nanocatalyst employing (a) a 10 ML defect-poor MgO film; (b) a 10 ML defect-rich MgO film. Markers show the experimental data points, the line represents a multipeak Gaussian fit to the data. Reprinted from Ref. [9] with permission of The American Chemical Society.

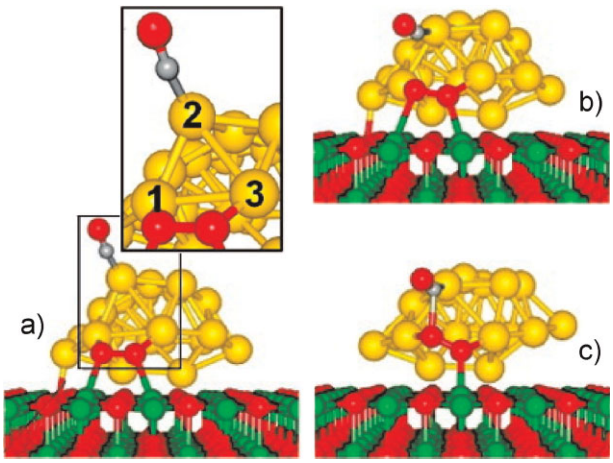

Figure 17 (online colour at: www.pss-b.com) Snapshots of a low temperature reaction pathway involving a bilayer Au_{20} cluster adsorbed on top of two neighboring oxygen vacancies on a thick MgO(100) surface. (a) The reaction starts from a peripherally adsorbed, peroxo-activated O_2 molecule and a CO molecule adsorbed on the bilayer gold cluster. (b) The barrier for the formation of the shown transition state CO–O_2 complex is 0.26 eV, and the dissociation process of the complex (c) entails an energy of 0.51 eV. The desorption of the product CO_2 molecule is found to be barrierless. In the inset in (a), Au atoms whose positions markedly distort during the reaction (i.e., exhibiting dynamic structural fluctionality) are designated as 1, 2, and 3. Color designation: Au atoms in yellow, C atoms in gray, O atoms in red, Mg atoms in green, and Mo atoms in black. Reprinted from Ref. [9] with permission of The American Chemical Society.

The joint experimental and theoretical investigations presented in this section demonstrate that the oxidation of CO at the gold nanoclusters sensitively depends on both, the thickness of magnesia film on Mo(100) as well as on the metal oxide stoichiometry, i.e., the surface defect density. These dependencies are reflected in variations of the reaction temperatures observed in the TPR experiments as well as in the amount of CO_2 produced. First principles simulations emphasize the importance of dimensionality changes for the observed changes in reactivity. In addition, the concept of dynamic structural fluctionality is illustrated. Most importantly, it is found that charge accumulation influences the active configuration and also defines the location of the reactive site on the cluster. Therefore, it can be concluded that catalytic reactivity can be tuned by variation of the properties, i.e., thickness and composition, of the supporting oxide ultrathin film.

5 Conclusion The aim of this contribution was to highlight the influence of the thickness and the composition of ultrathin metal oxide films on chemical reactions occurring at the surface of the oxide film and at metal clusters supported by the oxide film. Two different recent examples were chosen for this purpose, both employing ultrathin MgO(100) films grown on Mo(100) single crystals as substrate. Magnesia ultrathin films offer a versatile means for controlled variation of the electronic adsorbate–metal surface interaction via layer thickness and defect concentration. Influences on metal cluster and nanocatalytic reaction pathways have been observed to be pronounced for the first three magnesia monolayers. Particularly the metal cluster dimensionality is strongly influenced by charging phenomena occurring in the case of the very thin *albeit* defect-free MgO films. This fundamentally changes the catalytic reaction pathways. In addition, also the binding energies of the reactants and products, CO and CO_2, have been found to be influenced by the layer thickness.

Charging of the supported metal clusters has also been identified to be a key issue in the adsorption on oxygen vacancy defects on the magnesia surface [72, 74]. The effect of surface defects on the photoreaction dynamics of adsorbate molecules on magnesia thin films could be observed in fs time-resolved experiments as well. For the future, it is envisaged to combine surface femtochemistry investigations with nanocatalysis to gain insight into the fundamental events of bond making and bond breaking in elementary catalytic reactions.

Acknowledgements M.E.V. thanks the DAAD for a fellowship. T.M.B. is grateful for financial support by the Deutsche Forschungsgemeinschaft through the priority programs SPP 1153 "Clusters at surfaces," SFB 569 "Hierarchical structure formation and function in organic-inorganic nanosystems," and through grant BE2475/3. U.H. acknowledges financial support by the Deutsche Forschungsgemeinschaft through the priority program SPP 1153 "Clusters at surfaces." The work of U.L. and his group was supported by the US AFOSR and the DOE.

References

[1] V. E. Henrich and P. A. Cox, The Surface Science of Metal Oxides (Cambridge University Press, Cambridge, 1996).
[2] H.-J. Freund, Faraday Discuss. **114**, 1 (2000). U. Heiz and W.-D. Schneider, J. Phys. D **33**, R85 (2000).
[3] U. Heiz and U. Landman (eds.), Nanocatalysis (Springer-Verlag, Berlin, 2007).
[4] S. C. Street, C. Xu, and D. W. Goodman, Annu. Rev. Phys. Chem. **48**, 43 (1997).
[5] H.-J. Freund and D. W. Goodman, Ultrathin Oxide Films, in: Handbook of Heterogeneous Catalysis, Vol. 3, edited by G. Ertl, E. Knözinger, and F. Schüth (Wiley-VCH, Weinheim, 2008), p. 1309.
[6] S. Schintke, S. Messerli, M. Pivetta, F. Patthey, L. Libioulle, M. Stengel, A. De Vita, and W.-D. Schneider, Phys. Rev. Lett. **87**, 276801 (2001).
[7] S. Schintke and W.-D. Schneider, J. Phys.: Condens. Matter **16**, R49 (2004).
[8] H.-J. Freund and G. Pacchioni, Chem. Soc. Rev. **37**, 2224 (2008).
[9] C. Harding, V. Habibpour, S. Kunz, A. N.-S. Farnbacher, U. Heiz, B. Yoon, and U. Landman, J. Am. Chem. Soc. **131**, 538 (2009).
[10] L. Giordano, F. Cinquini, and G. Pacchioni, Phys. Rev. B **73**, 045414 (2005).
[11] M. E. Vaida, T. Gleitsmann, R. Tchitnga, and T. M. Bernhardt, J. Phys. Chem. C **113**, 10264 (2009).
[12] D. Ricci, A. Bongiorno, G. Pacchioni, and U. Landman, Phys. Rev. Lett. **97**, 036106 (2006).
[13] T. König, G. H. Simon, H.-P. Rust, and M. Heyde, J. Phys. Chem. C **113**, 11301 (2009).
[14] C. Zhang, B. Yoon, and U. Landman, J. Am. Chem. Soc. **129**, 2228 (2007).
[15] G. Pacchioni, L. Giordano, and M. Baistrocchi, Phys. Rev. Lett. **94**, 226104 (2005).
[16] P. Frondelius, A. Hellman, K. Honkala, H. Häkkinen, and H. Grönbeck, Phys. Rev. B **78**, 085426 (2008).
[17] H. Grönbeck, J. Phys. Chem. B **110**, 11977 (2006).
[18] M. Sterrer, T. Risse, U. Martinez Pozzoni, L. Giordano, M. Heyde, H.-P. Rust, G. Pacchioni, and H.-J. Freund, Phys. Rev. Lett. **98**, 096107 (2007).
[19] J. Wollschläger, J. Viernow, C. Tegenkamp, D. Erdös, K. M. Schröder, and H. Pfnür, Appl. Surf. Sci. **142**, 129 (1999). S. Valeri, S. Altieri, A. di Bona, C. Giovanardi, and T. S. Moia, Thin Solid Films **400**, 16 (2001).
[20] M. Sterrer, M. Heyde, M. Novicki, N. Nilius, T. Risse, H.-P. Rust, G. Pacchioni, and H. J. Freund, J. Phys. Chem. B **110**, 46 (2006).
[21] M.-C. Wu, J. S. Corneille, C. A. Estrada, J.-W. He, and D. W. Goodman, Chem. Phys. Lett. **182**, 472 (1991).
[22] M.-C. Wu, J. S. Corneille, J.-W. He, C. A. Estrada, and D. W. Goodman, J. Vac. Sci. Technol. A **10**, 1467 (1992).
[23] J. S. Corneille, J.-W. He, and D. W. Goodman, Surf. Sci. **306**, 269 (1994).
D. Ochs, W. Maus-Friedrichs, M. Brause, J. Günster, V. Kempter, V. Puchin, A. Shluger, and L. Kantorovich, Surf. Sci. **365**, 557 (1996).
M. C. Gallagher, M. S. Fyfield, J. P. Cowin, and S. A. Joyce, Surf. Sci. **339**, L909 (1995).
H.-M. Benia, P. Myrach, and N. Nilius, New J. Phys. **10**, 013010 (2008).

H. M. Benia, N. Nilius, and H.-J. Freund, Surf. Sci. **601**, L55 (2007).
[24] U. Heiz, F. Vanolli, L. Trento, and W.-D. Schneider, Rev. Sci. Instrum. **68**, 1986 (1997).
[25] M. C. Gallagher, M. S. Fyfield, L. A. Bumm, J. P. Cowin, and S. A. Joyce, Thin Solid Films **445**, 90 (2003).
[26] S. Benedetti, H. M. Benia, N. Nilius, S. Valeri, and H. J. Freund, Chem. Phys. Lett. **430**, 330 (2006).
[27] S. Benedetti, P. Torelli, S. Valeri, H. M. Benia, N. Nilius, and G. Renaud, Phys. Rev. B **78**, 195411 (2008).
[28] A. Kolmakov, J. Stultz, and D. W. Goodman, J. Chem. Phys. **113**, 7564 (2000).
[29] S. Wendt, Y. D. Kim, and D. W. Goodman, Prog. Surf. Sci. **74**, 141 (2003).
[30] G. Butti, M. I. Trioni, and H. Ishida, Phys. Rev. B **70**, 195425 (2004).
S. Prada, U. Martinez, and G. Pacchioni, Phys. Rev. B **78**, 235423 (2008).
[31] H.-J. Freund, Surf. Sci. **601**, 1438 (2007).
[32] M. Bieletzki, T. M. Soini, C. R. Henry, F. Esch, C. Barth, and U. Heiz, (in press).
[33] S. Valeri, S. Altieri, A. di Bona, P. Luches, C. Giovanardi, and T. S. Moia, Surf. Sci. **507–510**, 311 (2002).
[34] J. Wollschläger, D. Erdös, and K.-M. Schröder, Surf. Sci. **402–404**, 272 (1998).
[35] L. Plucinski, Y. Zhao, B. Sinkovic, and E. Vescovo, Phys. Rev. B **75**, 214411 (2007).
[36] C. Barth and C. R. Henry, Nanotechnology **17**, S155 (2006).
[37] C. Barth and C. R. Henry, J. Phys. Chem. C **113**, 247 (2009).
[38] S. Kitamura and M. Iwatsuki, Appl. Phys. Lett. **72**, 3154 (1998).
[39] C. Tegenkamp, H. Pfnür, N. Ernst, U. Malaske, J. Wollschläger, D. Peterka, K. M. Schröder, V. Zielasek, and M. Henzler, J. Phys.: Condens. Matter **11**, 9943 (1999). J. Kramer, W. Ernst, C. Tegenkamp, and H. Pfnür, Surf. Sci. **517**, 87 (2002).
[40] M. Sterrer, E. Fischbach, T. Risse, and H.-J. Freund, Phys. Rev. Lett. **94**, 186101 (2005).
[41] Z. Yan, S. Chinta, A. A. Mohamed, J. P. Fackler, Jr. and D. W. Goodman, J. Am. Chem. Soc. **127**, 1604 (2005).
[42] M.-C. Wu, C. M. Truong, and D. W. Goodman, Phys. Rev. B **46**, 12688 (1992).
[43] D. 1Peterka, C. Tegenkamp, K. M. Schröder, W. Ernst, and H. Pfnür, Surf. Sci. **431**, 146 (1999).
[44] C. Di Valentin, G. Pacchioni, S. Abbet, and U. Heiz, J. Phys. Chem. B **106**, 7666 (2002).
[45] C. Di Valentin, G. Pacchioni, M. Chiesa, E. Giamello, S. Abbet, and U. Heiz, J. Phys. Chem. B **106**, 1637 (2002).
[46] G. Pacchioni, ChemPhysChem **4**, 1041 (2003).
[47] G. Pacchioni and P. Pescarmona, Surf. Sci. **412/413**, 657 (1998).
[48] M. Sterrer, E. Fischbach, M. Heyde, N. Nilius, H.-P. Rust, T. Risse, and H. J. Freund, J. Phys. Chem. B **110**, 8665 (2006).
[49] P. V. Sushko, J. L. Gavartin, and A. L. Shluger, J. Phys. Chem. B **106**, 2269 (2002).
L. Giordano, U. Martinez, G. Pacchioni, M. Watkins, and A. L. Shluger, J. Phys. Chem. C **112**, 3857 (2008).
[50] M. Dynna, J. L. Vassent, A. Marty, and B. Gilles, J. Appl. Phys. **80**, 2650 (1996).
[51] J. Wollschläger, D. Erdös, H. Goldbach, R. Höpken, and K. M. Schröder, Thin Solid Films **400**, 1 (2001).
[52] M. E. Vaida, P. E. Hindelang, and T. M. Bernhardt, J. Chem. Phys. **129**, 011105 (2008).
[53] M. Vaida and T. M. Bernhardt, Eur. J. Phys. D **52**, 119 (2009).
[54] G. Li and H. J. Hwang, J. Chem. Phys. **124**, 244306 (2006). C. Hu, S. Pei, Y.-L. Chen, and K. Liu, J. Phys. Chem. A **111**, 6813 (2007).
[55] J. L. Knee, L. R. Khundkar, and A. H. Zewail, J. Chem. Phys. **83**, 1996 (1985).
L. R. Khundkar and A. H. Zewail, Chem. Phys. Lett. **142**, 426 (1987).
D. P. Zhong, P. Y. Cheng, and A. H. Zewail, J. Chem. Phys. **105**, 7864 (1996).
R. de Nalda, J. Durá, A. Garcia-Vela, J. G. Izquierdo, J. González-Vázquez, and L. Banares, J. Chem. Phys. **128**, 244309 (2008).
[56] D. P. Zhong and A. H. Zewail, J. Phys. Chem. A **102**, 4031 (1998). J. Durá, R. De Nalda, J. Álvarez, J. G. Izquierdo, G. A. Amaral, and L. Banares, ChemPhysChem **9**, 1245 (2008).
[57] R. de Nalda, J. G. Izquierdo, J. Durá, and L. Banares, J. Chem. Phys. **126**, 021101 (2007).
[58] A. B. Alekseyev, H.-P. Liebermann, R. J. Buenker, and S. N. Yurchenko, J. Chem. Phys. **126**, 234102 (2007).
[59] A. B. Alekseyev, H.-P. Liebermann, and R. J. Buenker, J. Chem. Phys. **126**, 234103 (2007).
[60] J. Kutzner, G. Lindeke, K. H. Welge, and D. Feldmann, J. Chem. Phys. **90**, 548 (1989).
K. A. Trentelman, D. H. Fairbrother, P. C. Stair, P. G. Strupp, and E. Weitz, J. Vac. Sci. Technol. A **9**, 1820 (1991).
K. A. Trentelman, D. H. Fairbrother, P. G. Strupp, P. C. Stair, and E. Weitz, J. Chem. Phys. **96**, 9221 (1992).
D. H. Fairbrother, K. A. Trentelman, P. G. Strupp, P. C. Stair, and E. Weitz, J. Vac. Sci. Technol. A **10**, 2243 (1992).
D. H. Fairbrother, K. A. Briggman, P. C. Stair, and E. Weitz, J. Phys. Chem. **98**, 13042 (1994).
D. H. 1Fairbrother, K. A. Briggman, P. C. Stair, and E. Weitz, J. Chem. Phys. **102**, 7267 (1995).
K. A. Briggman, P. C. Stair, and E. Weitz, Chem. Phys. Lett. **334**, 1 (2001).
[61] J. Y. Fang and H. Guo, J. Chem. Phys. **101**, 5831 (1994). J. V. Setzler, Z. H. Huang, and H. Guo, J. Chem. Phys. **103**, 4300 (1995).
[62] H. Guo and G. C. Schatz, Chem. Phys. Lett. **184**, 245 (1991).
[63] R. S. Mulliken, J. Chem. Phys. **8**, 382 (1940).
[64] J. W. Hudgens, T. G. DiGiuseppe, and M. C. Lin, J. Chem. Phys. **79**, 571 (1983).
[65] J.-Y. Fang and H. Guo, Chem. Phys. Lett. **235**, 341 (1995).
[66] M. A. Henderson, G. E. Mitchell, and J. M. White, Surf. Sci. **184**, L325 (1987).
M. X. Yang, S. K. Jo, A. Paul, L. Avila, B. E. Bent, and K. Nishikida, Surf. Sci. **325**, 102 (1995).
[67] V. P. Holbert, S. J. Garrett, J. C. Bruns, P. C. Stair, and E. Weitz, Surf. Sci. **314**, 107 (1994).
[68] M. Haruta, T. Kobayashi, H. Sano, and N. Yamada, Chem. Lett. 405 (1987).
M. Haruta, Catal. Today **36**, 153 (1997). M. Haruta and M. Daté, Appl. Catal. A **222**, 427 (2001).
[69] M. Haruta, Nature **437**, 1098 (2005).
[70] M. Haruta, Gold Bull. **37**, 27 (2004).

[71] M. Chen and D. W. Goodman, Oxide-Supported Metal Clusters, in: The Chemical Physics of Solid Surfaces, Vol. 12, edited by D. P. Woodruff (Elsevier, Amsterdam, 2007), p. 201.
D. W. Goodman, Dekker Encyclopedia of Nanoscience and Nanotechnology (Marcel Dekker, New York, 2004), p. 611.
R. Meyer, C. Lemire, S. K. Shaikhutdinov, and H.-J. Freund, Gold Bull. **37**, 72 (2004).
[72] A. Sanchez, S. Abbet, U. Heiz, W.-D. Schneider, H. Häkkinen, R. N. Barnett, and U. Landman, J. Phys. Chem. A **103**, 9573 (1999).
[73] H. Häkkinen, S. Abbet, A. Sanchez, U. Heiz, and U. Landman, Angew. Chem. Int. Ed. Engl. **42**, 1297 (2003).
[74] B. Yoon, H. Häkkinen, U. Landman, A. S. Wörz, J.-M. Antonietti, S. Abbet, K. Judai, and U. Heiz, Science **307**, 403 (2005).
[75] M. Sterrer, T. Risse, M. Heyde, H.-P. Rust, and H.-J. Freund, Phys. Rev. Lett. **98**, 206103 (2007).
V. Simic-Milosevic, M. Heyde, X. Lin, T. König, H.-P. Rust, M. Sterrer, T. Risse, N. Nilius, H.-J. Freund, L. Giordano, and G. Pacchioni, Phys. Rev. B **78**, 235429 (2008).
X. Lin, N. Nilius, H.-J. Freund, M. Walter, P. Frondelius, K. Honkala, and H. Häkkinen, Phys. Rev. Lett. **102**, 206801 (2009).
[76] V. Simic-Milosevic, M. Heyde, N. Nilius, T. König, H.-P. Rust, M. Sterrer, T. Risse, H.-J. Freund, L. Giordano, and G. Pacchioni, J. Am. Chem. Soc. **130**, 7814 (2008).
[77] B. Yoon and U. Landman, Phys. Rev. Lett. **100**, 056102 (2008).
[78] J. Li, H.-J. Zahi, and L.-S. Wang, Science **299**, 864 (2003).
[79] M. Tadjeddine, J. P. Flament, and C. Teichtel, Chem. Phys. **118**, 45 (1987).